Li_2MnO_3: A Catalyst for a Liquid Cl_2 Electrode in Low-Temperature Aqueous Batteries

Yiming Sui[1], Zengqing Zhuo[2], Ming Lei[3], Lu Wang[4], Mingliang Yu[1], Alexis M. Scida[1], Sean K. Sandstrom[1], William Stickle[5], Timothy D. O'Larey[1], De-en Jiang[3,*], Wanli Yang[2,*], and Xiulei Ji[1,*]

1. Department of Chemistry, Oregon State University, Corvallis, Oregon, 97331-4003, United States E-mail: david.ji@oregonstate.edu
2. Advanced Light Source, Lawrence Berkeley National Laboratory, Berkeley, California, 94720, United States E-mail: wlyang@lbl.gov
3. Department of Chemical and Biomolecular Engineering, Vanderbilt University, Nashville, Tennessee, 37235, United States E-mail: de-en.jiang@vanderbilt.edu
4. Department of Chemistry, University of California, Riverside, California, 92521, United States
5. Hewlett-Packard Co., 1000 NE Circle Blvd., Corvallis, Oregon, 97330, United States

Keywords: low temperature, chlorine, catalysis, Li_2MnO_3, aqueous batteries

Abstract

Li_2MnO_3 has been contemplated as a high-capacity cathode candidate for Li-ion batteries; however, it evolves oxygen during battery charging under ambient conditions, which hinders a reversible reaction. However, it is unclear if this irreversible process still holds under sub-ambient conditions. Here, we evaluated the low-temperature electrochemical properties of Li_2MnO_3 in an aqueous LiCl electrolyte and observed a reversible discharge capacity of 302 mAh/g at a potential of 1.0 V *vs.* Ag/AgCl at –78 °C with good rate capability and stable cycling performance, in sharp contrast to the findings in a typical Li_2MnO_3 cell cycled at room temperature. However, our results reveal that the capacity does not originate from the reversible oxygen oxidation in Li_2MnO_3 but the reversible $Cl_2(l)/Cl^-(aq.)$ redox from the electrolyte. Our results demonstrated the good catalytic properties of Li_2MnO_3 to promote the Cl_2/Cl^- redox at low temperatures.

1. Introduction

The parent compound of Li-rich layered metal oxides[1], *i.e.,* Li_2MnO_3, has garnered much interest due to its high Li contents and the associated high theoretical capacity values from potentially the oxygen redox reactions.[2] However, the materials suffer notorious capacity fading due to the almost completely irreversible oxygen oxidation in a typical battery cell at room temperature, especially during the initial charging, followed by low-capacity cycling primarily from the Mn (IV/III) redox reactions.[2a, 2b] In the meantime, the room temperature cycling behaviors indicated that Li_2MnO_3 is an effective catalyst through its very reactive surface, which could be potentially useful for novel electrochemical applications.[2b]

Considering the disadvantage of the highly irreversible oxygen oxidation at room temperature and the advantage of the highly reactive surface of Li_2MnO_3, we investigated the electrochemical properties of Li_2MnO_3 in an aqueous LiCl electrolyte at –78 °C. In sharp contrast to the room temperature behaviors, we observed a reversible discharge capacity of 302 mAh/g at a potential of 1.0 V *vs.* Ag/AgCl, a good rate performance with a capacity of 227 mAh/g retained at 200 mA/g, and good cycling stability of no capacity fading over 100 cycles with an average CE of 98%. Through a series of elemental sensitive characterization, we have confirmed that the oxygen oxidation in Li_2MnO_3 is "frozen" below –35 °C, while the reversible capacity originates from the Cl_2/Cl^- redox reaction catalyzed by the Li_2MnO_3 electrode. In addition, spectroscopic studies show that the surface of Li_2MnO_3 maintains its pristine Mn state, which again contrasts the room-temperature active behaviors and suggests a much more stable surface of Li_2MnO_3 as a catalyst at low temperatures. Further comparative study shows that the Li_2MnO_3 electrode catalyzes the Cl_2/Cl^- redox better than MnO_2, for which a mechanism is proposed.

2. Results and Discussions

2.1 Electrochemical Performance

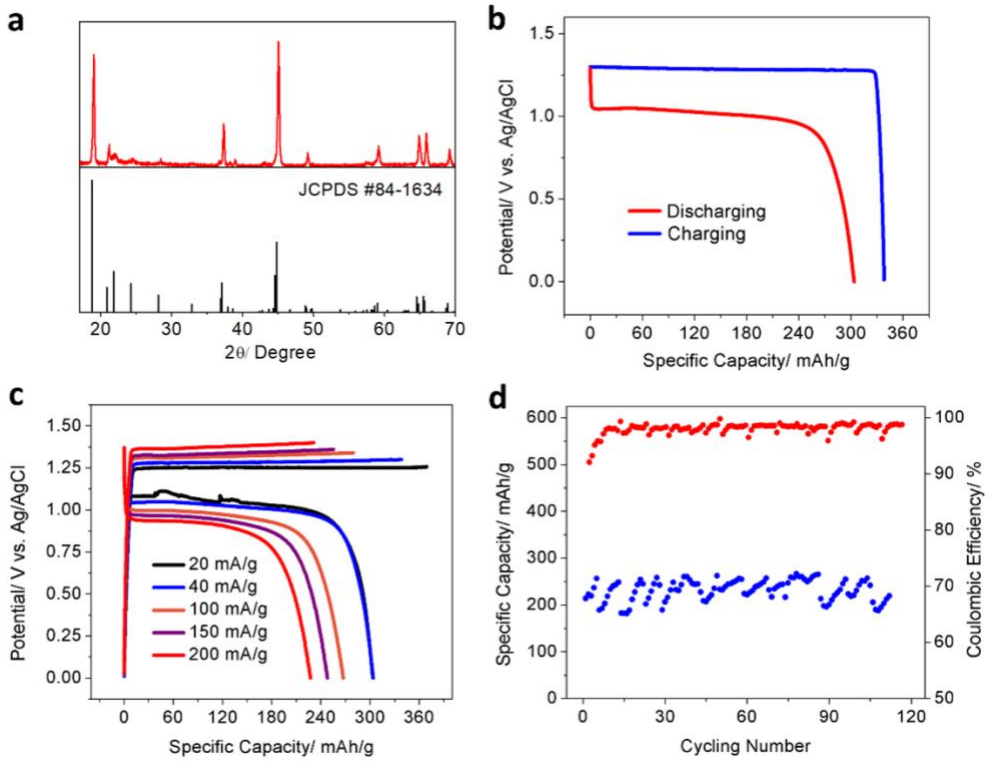

Figure 1. a) XRD pattern of the pristine Li_2MnO_3 electrode. b) GCD profiles of the Li_2MnO_3 electrode at –78 ℃ at a current rate of 40 mA/g, where the cutoff potentials are 0.0 V and 1.3 V *vs.* Ag/AgCl. c) GCD profiles for Li_2MnO_3 at –78 ℃ at various current rates. d) Cycling performance of the discharge capacity of Li_2MnO_3 at –78 ℃ at 80 mA/g.

Li_2MnO_3 is synthesized through a solid-state reaction at 800 ℃, with particle sizes ranging from ca. 100 nm to 250 nm (**Figure S1**). Li_2MnO_3 exhibits a monoclinic layered structure in a C2/m space group (JCPDS #26-1076) according to its X-ray diffraction (XRD) pattern (**Figure 1a**). We initially aimed to investigate whether the oxygen redox in Li_2MnO_3 is reversible at low temperatures. We first characterized the Li_2MnO_3 electrode by galvanostatic charge-discharge (GCD) cycling at a current rate of 40 mA/g at –78 ℃ in an aqueous electrolyte of 7 *m* (molality) LiCl. The first charge process of the Li_2MnO_3 electrode features a flat plateau at a potential of ca. 1.3 V (*vs.* Ag/AgCl, hereafter), and the following discharge also provides a nearly flat plateau at ca. 1.0 V, delivering a reversible capacity of 302 mAh/g,[3] where the Coulombic efficiency (CE) of the first cycle is 89% (**Figure 1b**). In addition, the Li_2MnO_3 electrode demonstrates excellent rate capability, where at the current rates of 20 mA/g, 40 mA/g, 100 mA/g, 150 mA/g, and 200

mA/g, the electrode offers high discharging capacity values of 303 mAh/g, 302 mAh/g, 267 mAh/g, 248 mAh/g, and 227 mAh/g, respectively (**Figure 1c**). The GCD results also suggest increased CE values from 82% to 89%, 97%, 98%, and 98%, correspondingly. When cycling at 200 mA/g, the electrode shows no capacity fading over 100 cycles with an average CE of 98% (**Figure 1d**). The capacity fluctuation is due to the temperature variations when dry ice was periodically added to the cold acetone bath to retain the low temperature.[4]

2.2 Working Mechanism of Li_2MnO_3 at Low Temperatures

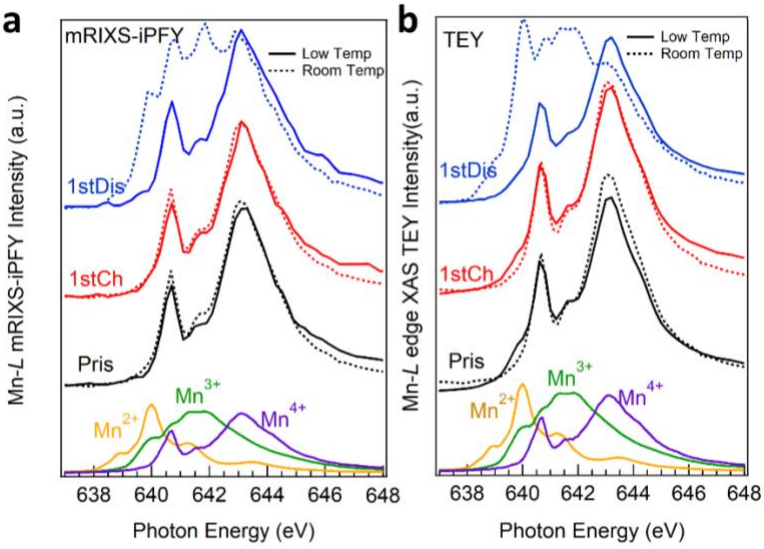

Figure 2. a) Mn L_3-edge mRIXS-iPFY spectra and b) Mn L_3-edge XAS-TEY spectra collected on Li_2MnO_3 samples cycled at the low temperature, (*i.e.*, –78 ℃, solid lines), compared with room-temperature cycled electrodes (dash lines)[2b], with $Mn^{2+}/Mn^{3+}/Mn^{4+}$ references plotted at the bottom. Technical details and Mn-*L* mRIXS of other samples are provided in the Supporting Information. Mn remains 4+ both in the bulk and on the surface throughout the low-temperature cycled samples, which is sharp contrast to any previously studied Li-rich electrodes, including Li_2MnO_3 (dashed lines), cycled at room temperature.

The reversible capacity observed from the Li_2MnO_3 electrode at –78 ℃ is intriguing. Prior studies revealed that at room temperature, the oxygen oxidation during the 1st charging is highly irreversible, and the Mn^{4+}/Mn^{3+} redox dominates the discharge capacity of Li_2MnO_3 after the first charging process.[2b], Therefore, we studied both the Mn-*L* and O-*K* edge soft X-ray mapping of

resonant inelastic X-ray scattering (mRIXS) and soft X-ray absorption spectroscopy (sXAS) of the Li_2MnO_3 electrodes at different state of charge (SOC) cycled at –78 °C (**Figure 2** and **3**). The Mn valence states in the Li_2MnO_3 electrode are evaluated both in the bulk and on the surface by employing the inverse partial fluorescence yield (iPFY) extracted from the Mn-*L* mRIXS experiments and the sXAS total electron yield (TEY), respectively. It should be mentioned that the mRIXS-iPFY has been well demonstrated for quantifying the Mn redox in battery electrodes with a probe depth of about 100 nm[5], while sXAS-TEY is known to be a surface probe with a probe depth of about 10 nm. The technical details are provided in the Supporting Information.

Figure 2a presents the mRIXS-iPFY spectra extracted from the mRIXS in **Figure S2**, and **Figure 2b** displays the TEY spectra. The valence state of Mn (solid lines in **Figure 2a** and **2b**) remains 4+ and unchanged both in the bulk and on the surface of all the electrodes cycled at –78 °C (solid lines). For a direct comparison, we plotted the results from room-temperature-cycled Li_2MnO_3 standard electrodes in **Figure 2a** and **2b** (dotted lines). The low-temperature-cycled electrodes displayed sharp contrasts to all the previous reports on Li-rich compounds cycled at room temperature in a typical battery cell, which always displayed highly reduced Mn^{2+} on the surface and significant amount of Mn^{3+} in the bulk of both Li-rich electrodes and Li_2MnO_3 (**Figure 2a**).[2b, 6]

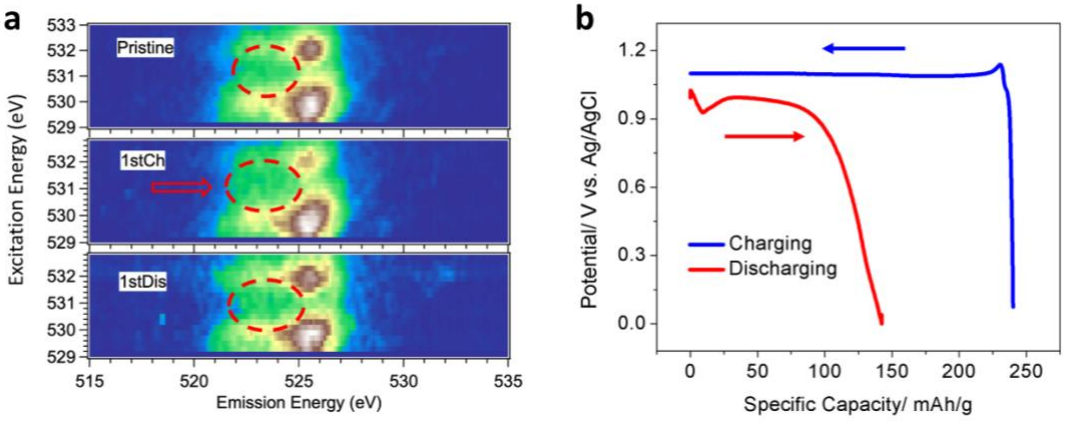

Figure 3. a) O *K*-edge mRIXS upon the excitation energy (horizontal axis) and the emission photon energy (vertical axis) of Li_2MnO_3 samples with different SOC, the pristine (b1), 1st fully charged (b2), and 1st fully discharged (b3) states. The dashed red circles indicate the typical

position of the fingerprint feature of oxidized oxygen that is missing here. b) GCD profiles of Li_2MnO_3 in the 2 *m* LiCl/DMF electrolyte at –35 ℃ at 200 mA/g, respectively.

With the unchanged Mn^{4+} state throughout the cycling, another natural speculation is whether the oxygen redox reaction, which is irreversible in room-temperature standard electrodes[2a, 2b], could be responsible for the low-temperature cycling with our aqueous electrolyte system. Therefore, we collected O *K*-edge mRIXS for the Li_2MnO_3 electrode at different SOC cycled at –78 ℃. As demonstrated in many previous studies, mRIXS could fingerprint the lattice oxidized oxygen through two specific signatures, with the clearest one at around 531 eV excitation and 524 eV emission energies.[7] However, no reversible features of the oxidized lattice oxygen can be observed in **Figure 3a**.

In another control experiment, Li_2MnO_3 is charged with a capacity of 200 mAh/g in an aqueous electrolyte of 10 *m* lithium bis(trifluoromethanesulfonyl)imide (LiTFSI) at room temperature, which should have removed most of the redox-active oxygen atoms of Li_2MnO_3 and Li-ions (**Figure S3**). XPS results reveal the weakened Li 1s peak in the charged Li_2MnO_3 electrode, suggesting that the charge process effectively oxidizes Li_2MnO_3 (**Figure S4**). The pre-charged Li_2MnO_3 electrode is collected and charged again in a different electrolyte of 7 *m* LiCl at –78 ℃. As shown in **Figure S5**, the pre-charged Li_2MnO_3 still exhibits a large reversible capacity of 274 mAh/g and the plateau behavior at –78 ℃, albeit with a larger extent of polarization at a rate of 40 mA/g. The results suggest that the oxygen redox unlikely contributes to the observed capacity of the Li_2MnO_3 electrode at –78 ℃.

As a matter of fact, the irreversible oxygen oxidation of standard Li_2MnO_3 electrodes cycled at room temperature always triggers severe structural degradation after just one charging cycle.[2a, 2b, 8] In contrast, after cycling at –78 ℃, the structure of the Li_2MnO_3 electrode remains intact, as shown by the comparative XRD patterns of the pristine electrode and the electrode after six cycles at 40 mA/g (**Figure S6**). The GCD potential profiles also display the same plateau behavior in the subsequent cycles as in the first cycle (**Figure S7**). All these chemical and structural observations here self-consistently indicated that the redox mechanism is completely different between electrodes cycled at –78 ℃ in aqueous electrolyte and those standard electrodes at room temperature. The low-temperature-cycled Li_2MnO_3 in the aqueous electrolyte displayed a

strikingly stable chemical and structural state throughout the high-capacity cycling, which is not expected for any intercalation type of battery electrodes.

In order to clarify the intriguing cycling mechanism, we further tested several electrochemical systems. The Li_2MnO_3 electrode delivers no reversible electrochemical behaviors in two non-chloride electrolytes, including a 5.2 *m* LiTFSI aqueous electrolyte[9] and a nonaqueous electrolyte of 1 M lithium bis(fluorosulfonyl)imide (LiFSI) plus 0.3 M $LiNO_3$ in 1,2-dimethoxyethane (DME)[10] at –35 °C, even charged to 1.6 V vs. Ag/AgCl (**Figure S8** and **S9**). However, at –35 °C, the Li_2MnO_3 electrode delivers a reversible discharge capacity of 150 mAh/g with a plateau at 1.1 V in the aqueous 7 *m* LiCl (**Figure S10**). Furthermore, the Li_2MnO_3 electrode demonstrates similar plateau GCD profiles as in LiCl at –78 °C in another two chloride-containing electrolytes, including the aqueous 7.5 *m* $ZnCl_2$[11] at –78 °C and a nonaqueous electrolyte of 2 *m* LiCl in dimethylformamide (DMF) at –35 °C (**Figure S11** and **3b**).[11] It should be mentioned that these electrolytes are selected because (1) they remain liquid at the low testing temperatures, (2) their ionic conductivities are comparable with the LiCl electrolyte at the testing temperatures, and (3) they cover two pertinent aspects: the choice of anions and the nature of electrolyte—aqueous or nonaqueous. The above disparate results suggest that the oxygen oxidation in Li_2MnO_3 is "frozen" at low temperatures. To understand this phenomenon, we conducted *ab initio* molecular dynamics (AIMD) simulations of the (010) surface of Li_2MnO_3 (**Figure S12**) at –78 °C and room temperature and found that the surface Mn-O bond lengths are, on average, 3% or 0.06 Å shorter at –78 °C than that at room temperature (**Figure S13**). A shorter bond length indicates higher covalency of the Mn-O bonds, thus inhibiting the oxygen evolution and the Mn redox in Li_2MnO_3 at low temperatures.[7a]

In addition, the results suggest the predominant role of Cl^- from the electrolytes in the reversible redox behavior of the Li_2MnO_3 electrode at low temperatures. We collected the Cl *L*-edge mRIXS-iPFY spectra for Li_2MnO_3 at different SOCs, where the Cl element is not detected in the bulk phase of all the electrodes, thus precluding the (de)insertion of Cl^-/Cl in the lattice of Li_2MnO_3 (**Figure S14**), which is consistent with the observed stable chemical and structural states discussed above.

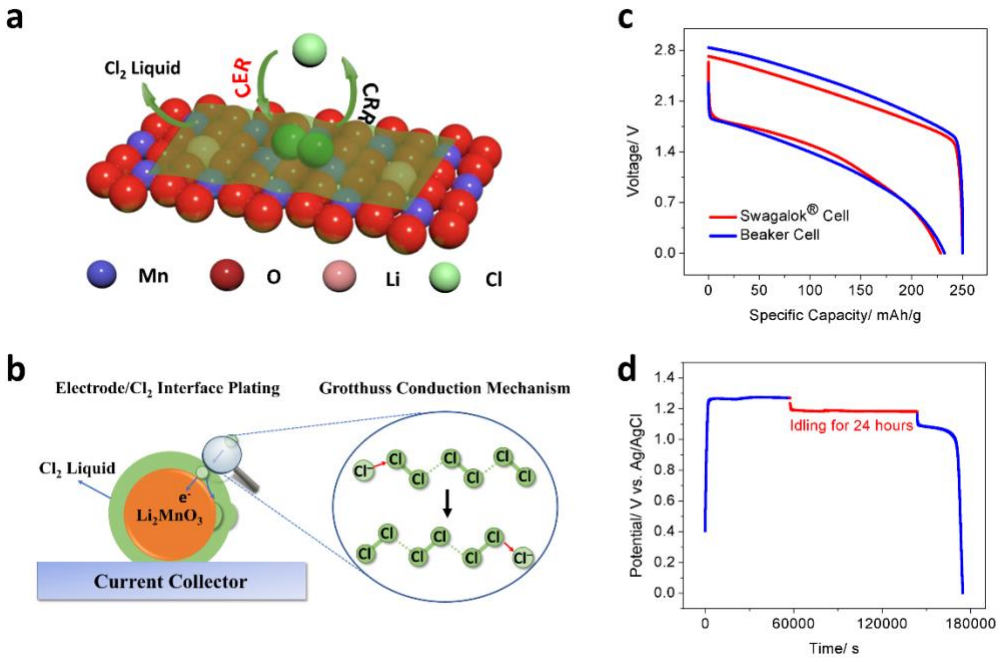

Figure 4. a) Schematic illustration of Cl_2/Cl^- redox over the Li_2MnO_3 surface at low temperatures. b) Schematic illustration of Cl^- conduction mechanism in the as-formed Cl_2 liquid. c) GCD profiles of the Li_2MnO_3 (mass loading of 2 mg) working electrode tested in in a two-electrode Swagelok® cell and a beaker cell with the AC counter electrode (active mass loading of 20 mg/cm^2) at a rate of 40 mA/g at –78 °C. d) GCD profiles of the Li_2MnO_3 electrode cycling at –78 °C at a rate of 20 mA/g with a 24-hour idling period between charging and discharging processes.

Therefore, all results of our multimodal characterization have pointed to a redox mechanism away from a conventional intercalation-type of cycling. We thus postulated a Cl_2/Cl^- redox mechanism that proceeds over the surface of the Li_2MnO_3 electrode. Li_2MnO_3 plays the dual role of (1) serving as a catalyst promoting both the chlorine evolution reaction (CER) and chlorine reduction reaction (CRR) and (2) supporting the as-formed Cl_2 liquid during the charging process (**Figure 4a**). It should be mentioned that the boiling point of Cl_2 liquid under atmospheric pressure is –34.6 °C, which is above the GCD test temperatures of –35 °C and –78 °C. Thus, the Cl_2 liquid can be "plated" over the cathode surface in the testing conditions.

Li_2MnO_3 delivers a high capacity of 288 mAh/g from the Cl_2/Cl^- reaction; however, it has a low Brunauer–Emmett–Teller (BET) surface area of 36 m^2/g (**Figure S15**). In contrast, we reported that activated carbon (AC) electrode with a high surface area of 2440 m^2/g delivers a

capacity of ca. 475 mAh/g under the same conditions (**Figure S16**).[12] The results suggest the storage of ca. 9-layer liquid Cl_2 (with a thickness of ca. 5 nm) over the Li_2MnO_3 particles (see **SI** for the calculation details).

As for the Cl_2 plating process, our hypothesis is that the electron holes on the interface between Li_2MnO_3 and the as-formed Cl_2 liquid combine with incoming Cl^- to form a new Cl_2 liquid layer beneath the existing layer. Such a plating process necessitates the charge conduction of Cl^- through the as-formed Cl_2 liquid (**Figure 4b**). Interestingly, the Cl^- conduction in Cl_2 liquid may benefit from the Grotthuss mechanism, which may explain the good kinetics of the Cl_2/Cl^- reaction at low temperatures.[13] (**Figure 4c**). In contrast to the conventional cathodes based on solid-state chemistry, the Li_2MnO_3 electrode serves as both the liquid Cl_2 plating substrate and the catalyst towards the Cl_2/Cl^- reaction. The unique mechanism prevents the occurrence of particle cracking and deformation typically associated with ion insertion/extraction, which explains the excellent cycling stability (**Figure 1d**).[14]

In addition, we studied whether the plated Cl_2 molecules on the Li_2MnO_3 electrode diffuse into the electrolyte, causing irreversible loss and self-discharge. Therefore, we collected the GCD profiles of the Li_2MnO_3 electrode in a two-electrode beaker cell at –78 °C, which exhibits similar capacity values as observed in the Swagelok® cells under the same conditions (**Figure 4d**). The self-discharging behavior of plated Cl_2 was further examined by idling a fully charged Li_2MnO_3 electrode for 24 hours at –78 °C before the subsequent discharging. The idled electrode exhibited a flat plateau but a smaller capacity of 171 mAh/g, corresponding to a CE of 53% (**Figure 4e**). The capacity loss is attributed to the disproportionation reaction between Cl_2 molecules and the aqueous electrolytes.[12]

2.3 Origin of the Excellent CER Performance over the Li_2MnO_3 Electrode

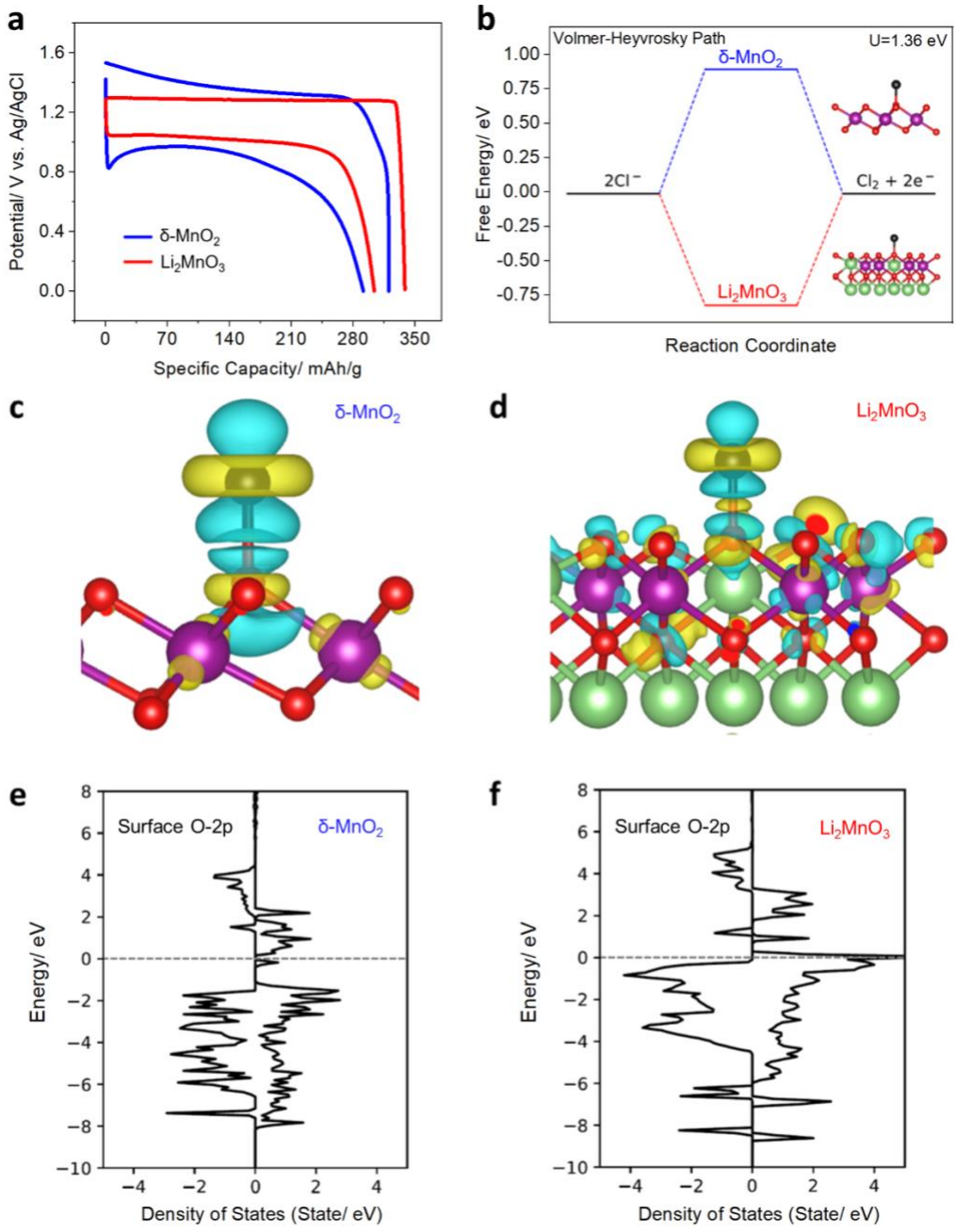

Figure 5. GCD profiles of a) δ-MnO_2 electrode and Li_2MnO_3 electrodes at −78 °C at a current rate of 40 mA/g. b) A DFT-calculated energy diagram of Cl* adsorption at the most stable sites on the (001) surfaces of δ-MnO_2 and Li_2MnO_3. The charge density difference analysis of adsorbed Cl on c) δ-MnO_2 and d) Li_2MnO_3; blue indicates electron-density accumulation and yellow suggests depletion. Color code: Cl, black; O, red; Mn, purple; Li, green. Density of states (DOS) of O-2p levels for the surface oxygen atoms in e) δ-MnO_2 and f) Li_2MnO_3, where the Fermi level is at 0 eV and +/- DOS denotes spin up/down contributions.

To study the factors that influence the CER catalytic activity of manganese oxide-based compounds, we conducted the galvanostatic tests on another manganese oxide compound, *i.e.,* δ-MnO_2 with the average particle size of 400 nm (**Figure S17**) and a surface area of 23 m^2/g (**Figure S18**). As shown in **Figure 5a**, δ-MnO_2 exhibits a larger extent of reaction polarization than that of Li_2MnO_3, indicating its poorer CER catalytic activity. The Mn L_3-edge mRIXS-iPFY and high-resolution Mn 2p3 XPS suggest that the dominant valence state of Mn is +4 in both Li_2MnO_3 and δ-MnO_2 (**Figure 2a**, **S19**).

Density functional theory (DFT) calculations were carried out to understand the energetics for CER on the (001) planes for both Li_2MnO_3 and δ-MnO_2 terminated with oxygen at the equilibrium potential of 1.36 V (**Figure S20**). We found that although Cl prefers to adsorb on top of an O atom on both surfaces, the adsorption energies are very different and opposite: it is favorable on Li_2MnO_3 but unfavorable on δ-MnO_2 (**Figure 5b**). To understand their adsorption energy differences, we calculated the charge density distribution of adsorbed Cl on the δ-MnO_2 (**Figure 5c**) and Li_2MnO_3 (**Figure 5d**) surfaces, where we observe a much stronger charge response to Cl adsorption on Li_2MnO_3. In addition, we calculated the local density of states (LDOS) of the surface O atoms on both δ-MnO_2 (**Figure 5e**) and Li_2MnO_3 (**Figure 5f**). One can see the O 2p level of Li_2MnO_3 shift up and its LDOS near the Fermi level is much greater than that of δ-MnO_2, which is consistent with the 0.18e less negative Bader charge on the surface O atom of Li_2MnO_3 than that of δ-MnO_2. The results suggest that the surface O on Li_2MnO_3 exhibits a stronger Cl adsorption, thus facilitating CER.

3. Conclusions

Li_2MnO_3 serves as a catalyst for a highly reversible redox reaction that forms Cl_2 liquid at –78 °C, which exhibits a discharge capacity of 302 mAh/g at a potential of 1.0 V in a 7 *m* LiCl aqueous electrolyte, along with good rate capability and stable cycling performance. By applying the mRIXS and sXAS, we can exclude the contribution of Mn and O redox in Li_2MnO_3; instead, the good performance is attributed to the Cl_2/Cl^- redox reaction on Li_2MnO_3. The low-temperature conditions stabilize the Li_2MnO_3 structure by suppressing the irreversible oxygen oxidation, which in turn avoids the severe chemical and structural instability occurred in standard Li_2MnO_3 electrodes cycled at room temperature. DFT calculations confirmed a favorable adsorption energy

of Cl atom on the O site of the Li_2MnO_3 surface. Our findings revealed a completely different cycling mechanism of Li_2MnO_3 at low temperatures and its catalytic properties for the chlorine evolution reaction.

4. Experimental Section/Methods

Materials and Synthesis: In this study, the Li_2MnO_3 is synthesized based on the solid-state reaction, as reported in the literature.[2b] The $LiOH \cdot H_2O$ powder (BioUltra >99%(T), Sigma-Aldrich Co., Ltd) and $MnCO_3$ powder (>99.9% trace metal basis, Sigma-Aldrich Co., Ltd) were mixed in the stoichiometric molar ratio of 2:1. The mixture was ball-milled in ethanol for 6 h and then centrifuged and dried at room temperature. The obtained precursor was finally annealed in a muffle furnace at the temperature of 800 ℃ for 20 h in air. The δ-MnO_2 is synthesized through the hydrothermal method. $KMnO_4$, 1.03 g, and 0.184 g $MnSO_4 \cdot H_2O$ are mixed in 25 ml DI water and then transferred to a 30 ml Teflon autoclave. After sealing, the autoclave is transferred to an oven, where it is heated at 160 ℃ for 12 h and naturally cooled down to room temperature. The product is centrifuged and washed with deionized water three times, and then it is dried at 80 ℃ for 12 h in air.

Electrode Preparation: The working electrode slurry is prepared by mixing active materials, *i.e.,* Li_2MnO_3, δ-MnO_2 with KetjenBlack (KB) and polyvinylidene fluoride (PVDF) (mass ratio of 7:2:1) in N-Methylpyrrolidone (NMP) solvent. The KB/PVDF electrode slurry is prepared by mixing KB and PVDF in a mass ratio 8:2 in NMP solvent. Then the slurry was cast over carbon fiber paper with an average active mass of 2.55 mg/cm^2. The counter electrodes are activated carbon (AC) free-standing films composed of 80 wt.% activated carbon and 20 wt.% polytetrafluoroethylene (PTFE) binder.

Materials Characterization: X-ray diffraction (XRD) was performed on a Rigaku Ultima IV diffractometer with Cu Kα radiation (λ = 1.5406 Å) to characterize the structure of electrodes. Soft X-ray Spectroscopy (SXS): Mn-*L* and O-K SXS measurement was performed in the iRIXS endstation at Beamline 8.0.1 of the Advanced Light Source (ALS) at Lawrence Berkeley National Laboratory (LBNL).[15] Mn-*L* X-ray absorption spectra (XAS) were collected at room temperature through the surface-sensitive total electron yield (TEY) mode with probe depth of less than 10nm.[16] Due to the notorious self-absorption effects, the utilization of Mn-*L* total fluorescence

yield is restricted, which is distorted at the $L_{2,3}$ peaks. In order to gain the bulk information, there is a method, inverse partial fluorescence yield extracted from the high efficiency mapping of resonant inelastic soft X-ray scattering (mRIXS-iPFY) introduced[7b], which is bulk sensitive with a probe depth of around 150 nm, and does not suffer from saturation or self-absorption effects. The whole mRIXS-iPFY measurement process was reported previously[2b] and is described as follows: Firstly, O-*K* normal x-ray emission spectrum (XES, 490-510 eV range with horizontal axis in **Figure S2**) was recorded by the high-efficiency mRIXS spectrometer through Mn-L_3 edge (vertical axis in **Figure S2**). Secondly, one partial fluorescence yield (PFY) was extracted by integrating the fluorescence intensity within the O-*K* XES energy range (490 to 510 eV) along the excitation energy (vertical axis in **Figure S2**). Finally, Mn-*L* iPFY was achieved through the inverse of the aforementioned PFY. It is important to note that because low-temperature *in-situ* soft X-ray experiments are unfortunately impossible at this time, all samples had to be taken out from the electrochemical cells and completely warmed up to room temperature for data collection. X-ray photoelectron spectroscopy (XPS) is equipped with a Physical Electrons Quantera Scanning ESCA Microprobe as well as a 1486.6 eV-power monochromatic Al Kα X-ray source for excitation.

Electrochemical Measurements: The half-cell measurement was conducted in Swagelok® three-electrode T-cells (1.3 cm diameter) with an Ag/AgCl (1 M HCl) reference electrode and titanium metal rods to support current collectors. The electrolytes were 7 *m* LiCl, 5.2 *m* LiTFSI, 7.5 *m* $ZnCl_2$ aqueous solutions, and 2 *m* LiCl in dimethylformamide (DMF) nonaqueous electrolyte without extra additives. The volume of the electrolyte is 2 mL, and the ratio of the electrolyte to the active material is 1 mL/mg. The nonaqueous electrolyte of 1 M lithium bis(fluorosulfonyl)imide plus 0.3 M $LiNO_3$ in 1,2-dimethoxyethane electrolyte (LiFSI-$LiNO_3$/DME) is tested in coin cells, which are assembled in a glove box filled with Argon and the concentrations of both O_2 and H_2O are controlled below 1 ppm. Glass microfiber filter papers served as the separators. The galvanostatic charge-discharge (GCD) and linear sweep voltammetry (LSV) tests were operated on an Arbin BT2000 battery cycler. The low-temperature measurements were conducted in Sanyo biomedical freezer at –35 ℃. For tests at –78 ℃, the cells were submerged in the CO_2 (s)/ethanol (l) mixture in a heat-insulating container.

Simulation: The calculations of bond lengths in Li_2MnO_3 at various temperatures were performed using DFT within the plane-wave pseudopotential as implemented in the VASP code[17] with a cutoff energy of 550 eV.[18] The exchange-correlation functional was described using the spin-polarized Perdew–Burke–Ernzerhof (PBE) functional.[19] The Hubbard U correction[20] (4.5 eV for Mn) was applied to the PBE to account for electron interactions on the 3d-electrons in the transition metals.[21] The k-space integrations were carried out utilizing the Monkhorst−Pack grid with 2 × 2 × 1 k-points in the Brillouin zone. The atomic positions were relaxed until the force on each atom was less than 0.05 eV/Å. Bulk Li_2MnO_3 forms a tetragonal lattice with space group C2/m, and experimental lattice constants are: a = 4.93 Å, b = 8.52 Å, c = 5.02. A $p(1 \times 1)$ periodic slab with 9 layers was built for Li_2MnO_3 (010). The bottom 3 layers were fixed. The vacuum gap thickness was set to be 15 Å. The model of the Li_2MiO_3 is shown in Figure S4. To determine the structural changes of Li_2MiO_3 at different temperatures. AIMD simulation was performed in the NVT ensemble employing Nosé–Hoover thermostats for 20 ps with 1 fs time step at 195 K and 298 K. We found that the surface structure is well equilibrated after 5ps and used the last 15 ps for bond-length analysis (Figure S13).

The DFT calculations for the energy diagram of Cl* adsorption on the surfaces of δ-MnO_2 and Li_2MnO_3 are performed with the Vienna *ab initio* simulation package (VASP 5.4.4) using projector-augmented waves (PAW) pseudopotentials and the exchange-correlation functionals parametrized by Perdew, Burke, and Ernzerhof for the generalized gradient approximation (GGA) with a cutoff energy of 500 eV. A Gaussian smearing with a width of 0.05 eV is used. The convergence criteria for energy and force are set as 10^{-5} eV and 0.01 eV·A^{-1}, respectively. Since PBE cannot correctly describe the d-d interaction of Mn, we adopt the PBE+U approximation with U-J = 4.0 eV.[7b] Our calculated relaxed lattice parameters are a=4.996 Å, b=8.627 Å and c=5.075 Å for Li_2MnO_3, and a=b=2.925 Å and c=17.408 Å for δ-MnO_2. The most stable surfaces of Li_2MnO_3 and δ-MnO_2 are the (001) surfaces. To model the Li_2MnO_3 (001) surface, we construct a four-layer slab with a vacuum layer of 15 Å applied in the z direction. The first two-layer and the adsorbates are fully relaxed with the bottom two-layer slabs fixed during the calculations. The Li_2MnO_3 (001) surface has two terminations, Li-terminated, and O-terminated surfaces. In our study, we focus on the O-terminated Li_2MnO_3 (001) surface since the surface environment of O-terminated Li_2MnO_3 (001) surface is very similar to that of the δ-MnO_2 (001) surface. The surface

energy of O-terminated Li_2MnO_3 (001) surface is 0.18 eV/Å^2, very close to the surface energy of Li-terminated surface 0.14 eV/ Å^2.

Surface energy is defined as:

$$\gamma = 1/2A(E_{slab} - N\ E_{bulk})$$

Here, A is the surface area, E_{slab} and E_{bulk} are the energy of the surface, and the bulk structure unit, respectively. N is the number of bulk structure units contained in the slab structure. A δ-MnO_2 (001) slab with a monolayer sandwich structure and a vacuum layer of 15 Å in the z direction are built to model δ-MnO_2 (001) surface.

For the chlorine evolution reaction, we assume the Cl_2 molecule formation via the same route as the hydrogen gas evolution reaction. At first, one Cl^- anion releases one electron to the electrode and forms the adsorbed Cl^* intermediate:

$$Cl^- + * \rightarrow Cl^* + e^-$$

The Gibbs free energy change ΔG(1) is:

$$\Delta G_1 = G(Cl^*) - \frac{1}{2}G(Cl_2) - G(*) - e(U - \varphi)\ (\varphi = 1.36\ eV)$$

Here, G(Cl^*), G(Cl_2), and G(*) are the energy of the surface with adsorbed Cl atom, isolated Cl_2 molecule, and pure surface, respectively. φ is the equilibrium potential of Cl_2/Cl^-, which is 1.36V. U is the electrode potential.

Next, another Cl^- attaches to the Cl^* and releases another electron to form an independent Cl_2 molecule.

$$Cl^- + Cl^* \rightarrow * + Cl_2 + e^-$$

The Gibbs free energy change ΔG(2) is:

$$\Delta G_2 = G(* + Cl_2) - G(Cl^*) - \frac{1}{2}G(Cl_2) - e(U - \varphi)$$

Here, G(*+Cl_2) is the energy of a pure surface with one isolated Cl_2 molecule.

We choose the DFT calculated energy as G and ignore the zero-point vibrational energy and entropy contribution, since our purpose is to compare the chlorine evolution reaction performance

on different electrode surfaces, and the zero-point vibrational energy and entropy contribution cancel each other out.

Mathematical Calculations: The calculation method is reported in our previous publication.[12] We suppose one Cl atom in a Cl_2 molecule contacts the electrode surface, so one Cl_2 molecule will occupy a surface area of ca. 9.6×10^{-20} m^2 on the Li_2MnO_3 electrode. The number of Cl_2 molecules (N_{cl2}) can be derived from the specific discharging capacity. In addition, we measured the BET surface area ($S_{electrode}$ with the unit of m^2/g) of Li_2MnO_3 particles, which is 36 m^2/g (**Figure S6**). Lastly, the amount of Cl_2 adsorption layer is derived through the equation:

$$Cl_2\ Layers = 9.6 \times 10^{-20} m^2 \times N_{Cl2}/S_{electrode}$$

Supporting Information

Supporting Information is available from the Wiley Online Library or from the author.

Acknowledgments

X. J. and D. J. thank the U.S. National Science Foundation (NSF) for the financial support with the Awards DMR 2221645 and DMR 2221646, respectively. This research used resources of the National Energy Research Scientific Computing Center, a DOE Office of Science User Facility supported by the Office of Science of the U.S. Department of Energy under contract no. DE-AC02-05CH11231. This research used resources of the Advanced Light Source, which is a DOE Office of Science User Facility under contract no. DE-AC02-05CH11231.

References

[1] a)J. Hong, W. E. Gent, P. Xiao, K. Lim, D.-H. Seo, J. Wu, P. M. Csernica, C. J. Takacs, D. Nordlund, C.-J. Sun, K. H. Stone, D. Passarello, W. Yang, D. Prendergast, G. Ceder, M. F. Toney, W. C. Chueh, *Nat. Mater.* **2019**, 18, 256; b)M. Sathiya, G. Rousse, K. Ramesha, C. P. Laisa, H. Vezin, M. T. Sougrati, M. L. Doublet, D. Foix, D. Gonbeau, W. Walker, A. S. Prakash, M. Ben Hassine, L. Dupont, J. M. Tarascon, *Nat. Mater.* **2013**, 12, 827.

[2] a)J. Rana, J. K. Papp, Z. Lebens-Higgins, M. Zuba, L. A. Kaufman, A. Goel, R. Schmuch, M. Winter, M. S. Whittingham, W. Yang, *ACS Energy Lett.* **2020**, 5, 634; b)Z. Zhuo, K. Dai, R. Qiao, R. Wang, J. Wu, Y.

Liu, J. Peng, L. Chen, F. Pan, Z.-x. Shen, *Joule* **2021**, 5, 975; c)M. Zhang, D. A. Kitchaev, Z. Lebens-Higgins, J. Vinckeviciute, M. Zuba, P. J. Reeves, C. P. Grey, M. S. Whittingham, L. F. Piper, A. Van der Ven, *Nat. Rev. Mater.* **2022**, 1; d)Z. Zhu, A. Kushima, Z. Yin, L. Qi, K. Amine, J. Lu, J. Li, *Nat. Energy* **2016**, 1, 16111.

[3] a)J. Lee, D. A. Kitchaev, D.-H. Kwon, C.-W. Lee, J. K. Papp, Y.-S. Liu, Z. Lun, R. J. Clement, T. Shi, B. D. McCloskey, *Nature* **2018**, 556, 185; b)H. Ji, J. Wu, Z. Cai, J. Liu, D.-H. Kwon, H. Kim, A. Urban, J. K. Papp, E. Foley, Y. Tian, *Nat. Energy* **2020**, 5, 213.

[4] Y. Sui, M. Yu, Y. Xu, X. Ji, *J. Electrochem. Soc.* **2022**, 169, 030537.

[5] K. Dai, J. Wu, Z. Zhuo, Q. Li, S. Sallis, J. Mao, G. Ai, C. Sun, Z. Li, W. E. Gent, W. C. Chueh, Y.-d. Chuang, R. Zeng, Z.-x. Shen, F. Pan, S. Yan, L. F. J. Piper, Z. Hussain, G. Liu, W. Yang, *Joule* **2019**, 3, 518.

[6] a)E. Hu, X. Yu, R. Lin, X. Bi, J. Lu, S. Bak, K.-W. Nam, H. L. Xin, C. Jaye, D. A. Fischer, K. Amine, X.-Q. Yang, *Nat. Energy* **2018**, 3, 690; b)J. Zhang, Q. Wang, S. Li, Z. Jiang, S. Tan, X. Wang, K. Zhang, Q. Yuan, S. J. Lee, C. J. Titus, K. D. Irwin, D. Nordlund, J. S. Lee, P. Pianetta, X. Yu, X. Xiao, X. Q. Yang, E. Hu, Y. Liu, *Nat. Commun.* **2020**, 11, 6342.

[7] a)Z. Zhuo, K. Dai, J. Wu, L. Zhang, N. Tamura, Y.-d. Chuang, J. Feng, J. Guo, Z.-x. Shen, G. Liu, *ACS Energy Lett.* **2021**, 6, 3417; b)W. Yang, T. P. Devereaux, *J. Power Sources* **2018**, 389, 188.

[8] R. Wang, X. He, L. He, F. Wang, R. Xiao, L. Gu, H. Li, L. Chen, *Adv. Energy Mater.* **2013**, 3, 1358.

[9] H.-I. Kim, E. Shin, S.-H. Kim, K. M. Lee, J. Park, S. J. Kang, S. So, K. C. Roh, S. K. Kwak, S.-Y. Lee, *Energy Storage Mater.* **2021**, 36, 222.

[10] W. Zhang, Y. Lu, L. Wan, P. Zhou, Y. Xia, S. Yan, X. Chen, H. Zhou, H. Dong, K. Liu, *Nat. Commun.* **2022**, 13, 2029.

[11] Q. Zhang, Y. Ma, Y. Lu, L. Li, F. Wan, K. Zhang, J. Chen, *Nat. Commun.* **2020**, 11, 4463.

[12] Y. Sui, M. Lei, M. Yu, A. Scida, S. K. Sandstrom, W. Stickle, T. D. O'Larey, D.-e. Jiang, X. Ji, *ACS Energy Lett.* **2023**, 8, 988.

[13] K. Iwamatsu, G. P. Horne, R. Gakhar, P. Halstenberg, B. Layne, S. M. Pimblott, J. F. Wishart, *Phys. Chem. Chem.* **2022**, 24, 25088.

[14] a)J. Li, S. Li, Y. Zhang, Y. Yang, S. Russi, G. Qian, L. Mu, S.-J. Lee, Z. Yang, J.-S. Lee, P. Pianetta, J. Qiu, D. Ratner, P. Cloetens, K. Zhao, F. Lin, Y. Liu, *Adv. Energy Mater.* **2021**, 11, 2102122; b)J. Li, N. Sharma, Z. Jiang, Y. Yang, F. Monaco, Z. Xu, D. Hou, D. Ratner, P. Pianetta, P. Cloetens, F. Lin, K. Zhao, Y. Liu, *Science* **2022**, 376, 517.

[15] R. Qiao, Q. Li, Z. Zhuo, S. Sallis, O. Fuchs, M. Blum, L. Weinhardt, C. Heske, J. Pepper, M. Jones, *Rev. Sci. Instrum.* **2017**, 88, 033106.

[16] W. Yang, X. Liu, R. Qiao, P. Olalde-Velasco, J. D. Spear, L. Roseguo, J. X. Pepper, J. D. Denlinger, Z. Hussain, *J. Electron Spectrosc. Relat. Phenom.* **2013**, 190, 64.

[17] a)G. Kresse, J. Furthmüller, *Comput. Mater. Sci.* **1996**, 6, 15; b)G. Kresse, J. Hafner, *Phys. Rev. B* **1994**, 49, 14251.

[18] F. Ning, B. Li, J. Song, Y. Zuo, H. Shang, Z. Zhao, Z. Yu, W. Chu, K. Zhang, G. Feng, *Nat. Commun.* **2020**, 11, 1.

[19] J. P. Perdew, K. Burke, M. Ernzerhof, *Phys. Rev. Lett.* **1996**, 77, 3865.

[20] V. I. Anisimov, J. Zaanen, O. K. Andersen, *Phys. Rev. B* **1991**, 44, 943.

[21] Z. Chen, J. Li, X. C. Zeng, *J. Am. Chem. Soc.* **2019**, 141, 10751.

TOC

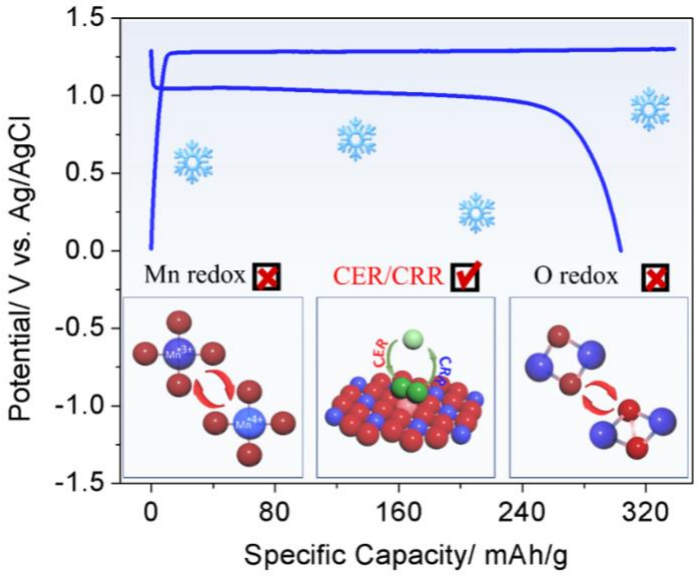

Below –35 °C, the anionic oxygen redox in Li_2MnO_3 is "frozen," thus not contributing to the observed capacity. However, at low temperatures, Li_2MnO_3 catalyzes a reversible redox reaction of $Cl_2(l)/Cl^-$ on its surface in aqueous 7 *m* LiCl.